

Femtofarad optoelectronic integration demonstrating energy-saving signal conversion and nonlinear functions

Kengo Nozaki^{1,2*}, Shinji Matsuo^{1,3}, Takuro Fujii^{1,3}, Koji Takeda^{1,3}, Akihiko Shinya^{1,2}, Eiichi Kuramochi^{1,2} and Masaya Notomi^{1,2*}

The introduction of photonic technologies into mature electronic circuits is in high demand to accelerate on-chip information networking and even computing. Great difficulty lies in the fact that the optoelectronic coupling at their interfaces requires a substantial charging energy determined by their capacitance. Optoelectronic devices have been too large to reduce the integrated capacitance down to the femtofarad scale. Here we use a photonic-crystal platform to demonstrate the first experimental proof of optoelectronic integration at only 2 fF. This allows us to realize a record-low attojoule-energy electro-optic modulator (an electrical-to-optical or E-O converter) and an amplifier-free photoreceiver (an optical-to-electrical, or O-E converter), which leads to ultralow-energy signal conversion. By integrating these O-E/E-O devices, we demonstrate femtofarad 'O-E-O transistors' with optical signal gain that show various optical nonlinear functions, including as all-optical switches, wavelength converters and cascable optical repeaters with a femtojoule-per-bit energy consumption. These femtofarad-scale O-E/E-O/O-E-O devices promise tightly coupled photonic-electronic integration for new fields of energy-saving information processing.

It is now recognized that the performance of computers that are based on complementary metal oxide–semiconductor (CMOS) technology is reaching its limit¹. The introduction of optics into computers is an understandable solution because we can fully enjoy the merits of both electronics and photonics while overcoming the demerits. Electric circuitry suffers from power-consuming signal transportation and resistance-capacitance (RC) delay, which becomes increasingly problematic as the bit rate increases. All-optical circuitry does not suffer from these effects, but it is restricted by intrinsically low nonlinearity and poor functionalities. Therefore, if we employ them in appropriate roles, we can expect to overcome the problems that arise with CMOS computers. The penetration of optics into computers began at relatively long distances (rack-to-rack, board-to-board), which became shorter and shorter. However, there are technical barriers to chip-scale optoelectronic integration. First, conventional optical-to-electrical (O-E) and electrical-to-optical (E-O) conversions require a large amount of energy (typically picojoules per bit), although the allowable energy in a chip is at the femtojoules-per-bit scale or lower^{2–4}. This issue—namely femtofarad-level optoelectronic integration—is now considered one of most important problems if we are to realize computers that are tightly coupled with photonics^{3,5–7}.

We recently demonstrated that the capacitance of photodetectors (PDs) can be greatly reduced to a sub-femtofarad regime by using artificial dielectric structures that exhibit strong light confinement, namely photonic crystals (PhCs)⁸. Here, we employ PhCs to challenge the above-mentioned problem. In this report, we first demonstrate an electro-optic modulator (EOM) with an ultrasmall capacitance (0.6 fF) by using PhC nanocavities operating at 40 Gbit s^{−1}. The energy consumption is as small as 42 aJ bit^{−1}, which is the lowest record for any type of EOM. Next, we demonstrate successful femtofarad-level O-E-O integration, in which a PD is electrically integrated with an EOM.

It has been known since the 1980s that O-E-O integration could lead to functional pseudo-optical nonlinear devices that are capable of operating as wavelength converters, optical switches or optical transistors^{9–12}. The nonlinearity can be enhanced by optoelectronic integration and this approach has the potential to solve some of the problems posed by all-optical devices, such as cascability or signal amplification. However, the performance of previous O-E-O devices was severely limited by RC delay and large energy consumption, primarily due to their large capacitance (>100 fF)^{9,13–15}. In this work, we solve this problem by the close integration of a fF-PD and a fF-EOM¹⁶. We have experimentally confirmed that the total capacitance is at the femtofarad level.

We demonstrate a number of functionalities of our O-E-O device, including as an efficient wavelength converter and an optical switch with an energy cost at the femtojoule-per-bit level. These results also offer the first experimental proof of amplifier-free photoreceiver operation using a small-capacitance PD. Our O-E-O device enables high optical nonlinear conversion with better-than-unity efficiency, which is difficult for pure all-optical nonlinear devices and is promising for cascable nonlinear processing. The present result shows that femtofarad optoelectronic integration can overcome various limitations found with solely electronic/photonic circuitry, and opens up photonic processing tightly combined with electronic circuits.

Results

Attojoule-per-bit nanocavity EOM. We demonstrate an E-O converter that has small capacitance and can be driven with ultralow electrical energy. A cavity-based approach has often been utilized for EOMs to reduce the operative signal voltage and capacitance^{6,17,18}. We employed an L3-type PhC nanocavity (a point defect with three airholes missing from a line), as shown in Fig. 1a (the design and

¹Nanophotonics Center, NTT Corporation, Atsugi, Japan. ²NTT Basic Research Laboratories, NTT Corporation, Atsugi, Japan. ³NTT Device Technology Laboratories, NTT Corporation, Atsugi, Japan. *e-mail: kengo.nozaki.f.d@hco.ntt.co.jp; masaya.notomi.mn@hco.ntt.co.jp

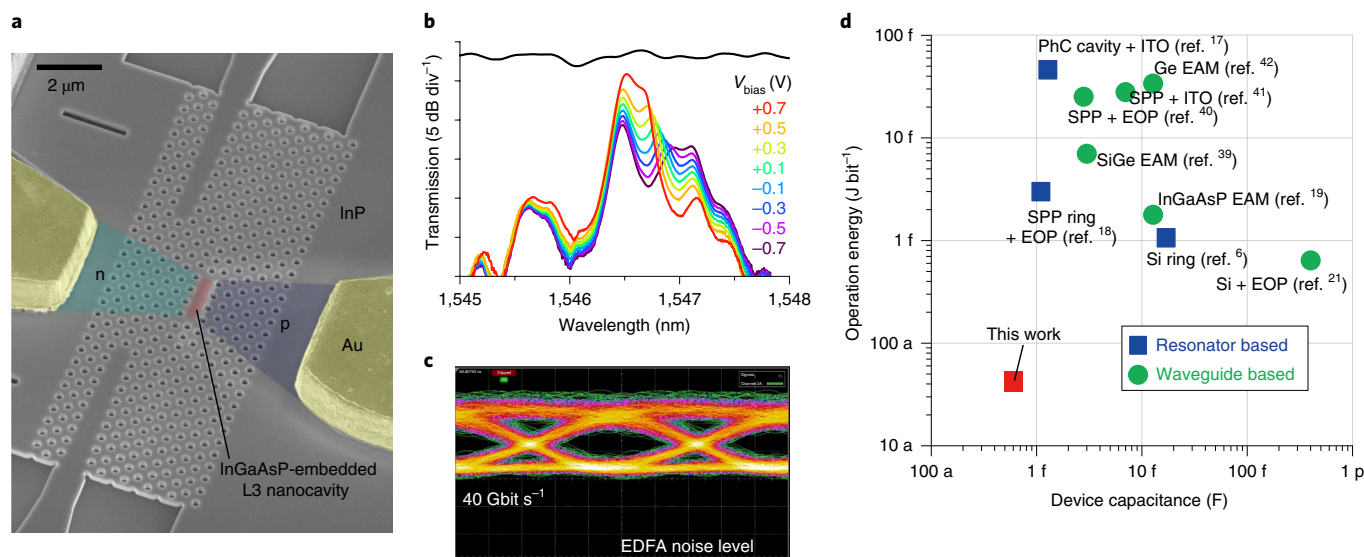


Fig. 1 | PhC-nanocavity EOM. **a**, Scanning electron microscope (SEM) image of the EOM. **b**, Transmission spectra for different d.c. bias voltages. The black curve denotes the reference waveguide. **c**, An eye diagram for a bit rate of 40 Gbit s⁻¹. A V_{bias} of +0.4 V and a V_{pp} of 0.5 V are applied. The extinction ratio is 2.4 dB. EDFA, erbium-doped fibre amplifier. **d**, Comparison of EOMs in terms of operation energy per bit and device capacitance^{6,17–19,21,39–42}. SPP, surface plasmon polariton; EOP, electro-optic polymer; EAM, electro-absorption modulator; ITO, indium tin oxide. For the numbers on the axes, a, f, and p denote atto, femto and pico, respectively.

fabrication of the device are described in Supplementary Section 1). This PhC-EOM has a theoretical capacitance (C_{EOM}) of only 0.6 fF (excluding the metal wires and pads), which is the same as that of PhC-PDs⁸. Because of the embedded InGaAsP, the internal electric field in the p–i–n junction induces an increased refractive index and optical absorption by the Franz–Keldysh effect (FKE)¹⁹. The resonant transmission, which has a cavity quality factor (Q) of 5,400 (full-width at half-maximum of about 0.3 nm), was suppressed and shifted by the voltage, as shown in Fig. 1b. The maximum transmission was observed at a forward bias voltage (V_{bias}) of +0.7 V due to the elimination of the built-in voltage of the p–i–n junction and the consequent suppression of the FKE.

Dynamic modulation at a bit rate of 40 Gbit s⁻¹ for a non-return-to-zero (NRZ) signal was successfully observed in the eye diagram in Fig. 1c, for which the V_{bias} was +0.4 V and the swing voltage (V_{pp}) was 0.5 V (see Supplementary Section 2). We estimated the dynamic energy consumption. The charging energy with the capacitance^{6,20,21} was only ~40 aJ bit⁻¹, whereas the external biasing energy was negligibly small at ~2 aJ bit⁻¹. It should be noted that the photocurrent dissipation energy, which is consumed in the reverse voltage range^{19,20}, is completely eliminated in our device when operated in the forward-biased condition (see Supplementary Section 3). Figure 1d compares the operation energy and capacitance in previous EOMs with various types of nonlinear materials and structures. Note that the operation energy of our PhC-EOM is over an order of magnitude smaller than that of other EOMs, and simultaneously exhibits extremely small capacitance. These two characteristics are highly attractive for an optical transmitter in an on-chip photonic link. As presented below, they also play a critical role in the O–E–O transistor function.

Femtofarad O–E–O coupling. As we have realized fF-PhC-PDs⁸ and fF-PhC-EOMs, we integrate them into an O–E–O device, as shown in Fig. 2a. It is worth noting that the device occupies a footprint of only 10 × 15 μm². A simulation revealed that the total capacitance ($C = C_{\text{PD}} + C_{\text{EOM}}$) is still as low as 1.64 fF (see Supplementary Section 4). Two parallel p-doped regions at the sides of the EOM work as a load resistor, and the combined resistance (R_{load}) is

24 kΩ. An isolated PhC-PD without a load resistor was evaluated separately, and a high responsivity (η_{pd}) of 1 A W⁻¹ and 40 Gbit s⁻¹ dynamics were confirmed (see Supplementary Section 5).

Figure 2b shows the operation scheme. An input optical signal with a peak power of P_{in} (W) and a wavelength of 1,550.0 nm is injected into the PD, and the generated photocurrent (I_{pd}) charges the device capacitance and is discharged via the load resistor. The EOM is driven by the photovoltage (V_{pho}), which was deduced by multiplying the measured photocurrent and R_{load} , as given by $V_{\text{pho}} = \eta_{\text{pd}} P_{\text{in}} R_{\text{load}}$. As shown in Fig. 2c, V_{pho} increases linearly with P_{in} , and saturates at around 1.4 V. In fact, this shows that a single p–i–n PD generates a photovoltage of over 1 V without using an electric amplifier. This demonstrates the realization of an amplifier-free photoreceiver, as discussed below.

Figure 2d shows the variation in the transmission spectra for an EOM under simultaneous continuous-wave (CW) light injection into a PD (see Supplementary Section 6 for the EOM without light injection into the PD). As V_{pho} increases, the resonant transmission of the EOM was suppressed and redshifted by the FKE. We note that the thermo-optic effect may play some role in this redshift, which is caused by joule heating at the load resistor. However, the dynamic modulation at high frequency (Fig. 3) is driven solely by the FKE because the thermo-optic effect cannot follow the speed. As shown in Fig. 2d, when the wavelength is set to resonance or longer wavelengths, we can choose the ‘normally on’ or ‘normally off’ operations, respectively. It is worth noting that these operations are analogous to a three-terminal transistor, if we assume that the light going into the PD and EOM are the gate voltage and the source voltage, respectively, and that the light output from the EOM is the drain voltage.

Dynamic all-optical modulation. Here we demonstrate all-optical dynamic modulation with our O–E–O transistor. This should provide direct proof of ultralow capacitance, because the RC limit governs the dynamic behaviour. As shown in Fig. 3a, an intensity-modulated optical signal and CW light (normally off condition) were injected into a PD and an EOM, respectively, and the output signal from the EOM was analysed (see Supplementary Section 7

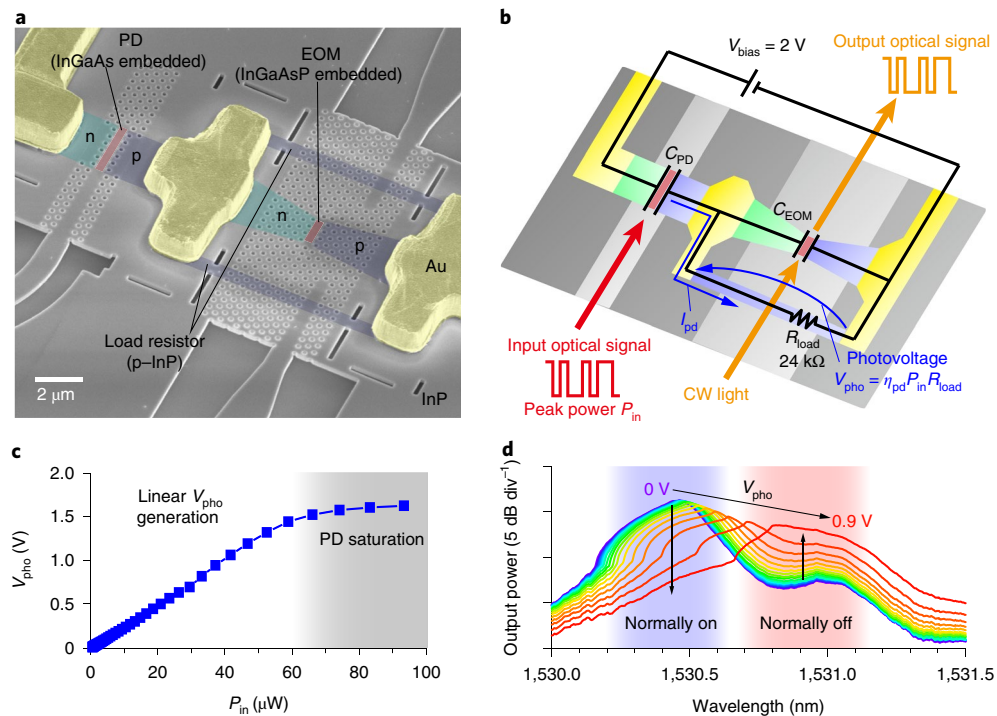


Fig. 2 | PD-EOM integration. **a**, SEM image of the device. An L3-nanocavity PhC-EOM (Fig. 1) and a 2.7- μm -long PhC-PD are closely integrated. Two parallel p-doped regions at the sides of the EOM work as a load resistor, and are utilized to block unintentional electrical conduction through the substrate between the n-doped regions. **b**, The operation scheme. Two parallel load resistors are merged in the schematic. An input optical signal with a peak power of P_{in} is converted to a photocurrent I_{pd} by the PD, and generates a photovoltage V_{pho} across the load resistor. The EOM is driven by V_{pho} . **c**, V_{pho} for P_{in} . **d**, The change of transmission spectrum for the EOM with V_{pho} .

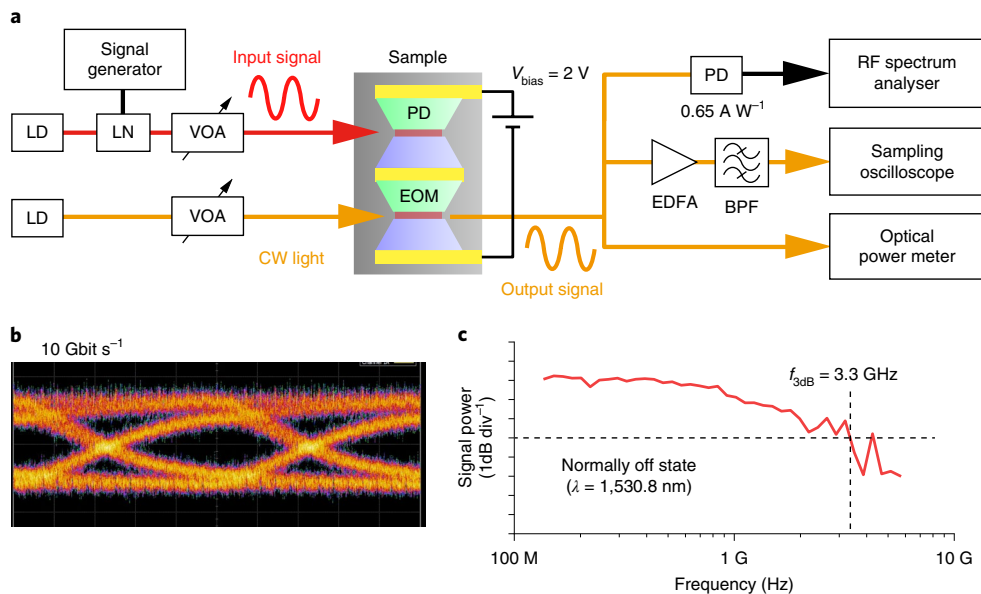


Fig. 3 | Operation dynamics for the O-E-O transistor. **a**, Measurement setup. Intensity-modulated optical signal ($\lambda = 1,550.0 \text{ nm}$) and CW light ($\lambda = 1,530.8 \text{ nm}$, normally off condition) were injected into the PD and the EOM, respectively. LD, laser diode; LN, lithium niobate modulator; VOA, variable optical attenuator; BPF, band-pass filter. **b**, An eye diagram for the NRZ signal. A pseudo-random bit sequence pattern with 2^{11} -1 bits is used. The modulation contrast is 1.5 dB. **c**, Frequency responses for the normally off condition. For the numbers on the bottom axis, M and G denote mega and giga, respectively.

for the detailed setup). An eye diagram for a bit rate of 10 Gbit s^{-1} was clearly observed, as shown in Fig. 3b. This is remarkably fast when we consider that R_{load} is $24 \text{ k}\Omega$. The input optical peak power (P_{in}) for the PD was approximately $32 \mu\text{W}$. When we account

for the half mark ratio of the bits '1' and '0' for the 10 Gbit s^{-1} pseudo-random bit sequence NRZ pattern, the average optical energy is only 1.6 fJ bit^{-1} . This is more than two orders of magnitude lower than those for previous O-E-O devices^{15,22,23}.

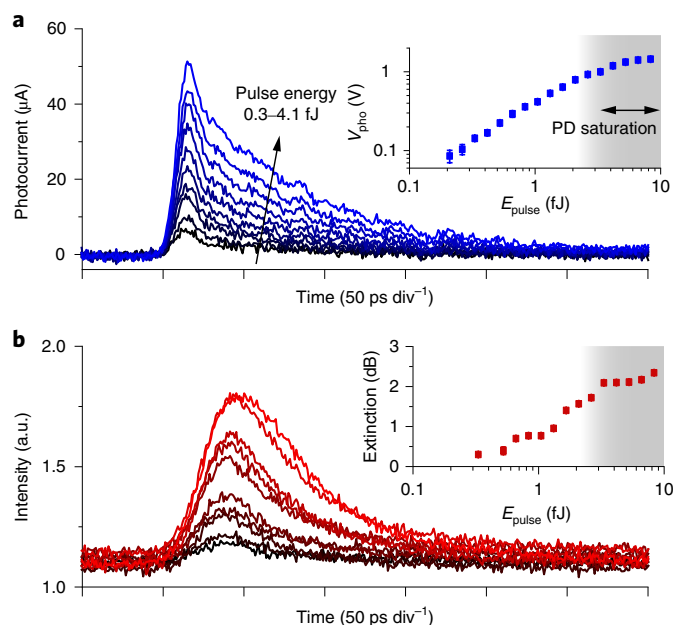


Fig. 4 | Short pulse response. **a**, Photocurrent response. E_{pulse} is changed from 0.3 to 4.1 fJ. The inset shows the generated V_{pho} for each E_{pulse} . The shaded area denotes the saturation region of the PD. **b**, Output signal response for EOM with normally off condition. The inset shows the extinction ratio for E_{pulse} .

Capacitance evaluation. High-speed and low-energy operations are attributed to the ultralow integrated capacitance. Thus, the capacitance measurement is important, but it is generally difficult to explicitly measure a femtofarad-level capacitance in a chip through external electrical probing because the pad-to-pad capacitance (~ 5 fF) should dominate the local device capacitance. However, our O–E–O device enables us to access the local capacitance directly by optical charging through the PD and optical probing through the EOM, and even femtofarad capacitances can be measured by analysing the all-optical dynamics. For this purpose, we employed a sinusoidal optical signal, and measured the frequency response as shown in Fig. 3c. This reveals a 3 dB bandwidth ($f_{3\text{dB}}$) of 3.3 GHz. As the carrier transit-time bandwidth (f_{TR}) was separately evaluated at 18 GHz (see Supplementary Section 8), $f_{3\text{dB}}$ is dominated by the RC bandwidth (f_{RC}) of 3.4 GHz. This implies that, depending on the application, $f_{3\text{dB}}$ and the operative bit rate can be varied by changing R_{load} up to the carrier transit-time limit. In the experiment, the device capacitance was determined to be $C = (2\pi R_{\text{load}} f_{\text{RC}})^{-1} = 2.0$ fF. This result agrees well with the theoretical value of $C = 1.64$ fF. This measured capacitance is two orders of magnitude lower than that for previous integrated O–E–O devices^{13,15}, and allows us to employ an ultralow optical energy of 1.6 fJ bit^{−1} for charging. We cannot over-emphasize the importance of this direct capacitance measurement of femtofarad optoelectronic integration, since such direct measurement has been difficult using conventional methods.

Short-pulse response. A 2-ps-wide optical pulse was also launched to characterize the charging energy and the dynamic V_{pho} . Figure 4a shows the instantaneous photocurrent response with an inset showing the photovoltage, deduced by multiplying the peak photocurrent by $R_{\text{load}} = 24$ k Ω . Although we observed some saturation in the d.c. measurement (see Fig. 2c), the dynamic V_{pho} still increases linearly up to 1 V at an optical pulse energy (E_{pulse}) of ~ 3 fJ. For the O–E–O transistor function, this V_{pho} should meet the driving level of the EOM. Figure 4b shows the transient response of the EOM output light. If we take the same extinction ratio (1.5 dB) as the NRZ

modulation in Fig. 3b, the E_{pulse} contribution to the device charging is as low as 1.9 ± 0.2 fJ, and V_{pho} is as high as 0.71 ± 0.08 V. The device capacitance can be also evaluated from E_{pulse} and V_{pho} and the result agrees well with the bandwidth measurement (see Supplementary Section 9).

Demonstration of the functionalities of the O–E–O transistor. **Amplifier-free photoreceiver.** As described above, our O–E–O transistor has various functionalities. The resistor-loaded PhC-PD, which is part of the O–E–O transistor, dynamically converts optical energy to voltage (Fig. 4a). This works as an amplifier-free photoreceiver, which can greatly reduce the energy consumption²⁴. Our previous work on a resistor-loaded PD revealed a light-to-voltage conversion efficiency (η_{LV}) at a kilovolts-per-watt scale, but the parasitic capacitance of more than 10 fF caused by the metal wiring increases the energy requirements to the 100 fJ level⁸. The present O–E–O integration with only 2 fF enables the demonstration of the amplifier-free receiver operation at a femtojoule level.

The efficiency-bandwidth product (EBP) is the figure of merit for the photoreceiver, and is given by $\eta_{\text{LV}} f_{3\text{dB}} \approx (2\pi C)^{-1}$ (in V J^{−1}) for the resistor-loaded PD (see Supplementary Section 10). With a 2 fF capacitance, our receiver operation exhibits an EBP of 8×10^{13} V J^{−1}. This value is comparable to those of cutting-edge CMOS receivers equipped with electrical amplifiers. The energy consumption, including both the optical and electrical components, is also an important property. Although CMOS receivers support a high EBP of 2×10^{14} V J^{−1} with integrated amplifiers, they require an electrical energy of several hundred femtojoules or picojoules per bit. Our resistor-loaded PD consumes only 3.2 fJ bit^{−1} as a result of the energy dissipation induced by the photocurrent and the reverse bias voltage (2 V)^{19,20}. The energy, including the optical component (1.6 fJ bit^{−1}), needed to generate 0.77 V is only 4.8 fJ bit^{−1}, which greatly outperforms existing CMOS receivers. This may enable a densely integrated receiver array on a chip.

Optical wavelength converter and switch with gain. As the wavelength of a PD input can be set independently from the EOM output, it functions as a wavelength converter. All-optical wavelength converters based on semiconductor waveguides, which utilize a cross-gain modulation²⁵ or a coherent parametric mixing²⁶, typically consume energy at the 100 fJ bit^{−1} to pJ bit^{−1} level, or as high as that of previously reported O–E–O devices^{15,22,23}. In our operation in Fig. 3, we demonstrated wavelength conversion from 1,550.0 to 1,530.8 nm with femtojoule-per-bit energy. The same device can be used as an all-optical switch, in which the control light switches the other light to be transmitted or blocked.

Here we evaluate the efficiency of the optical signal conversion for nonlinear applications. We measured the power ratio of an output sinusoidal signal to its input counterpart. Figure 5a shows the output optical signal power as a function of wavelength with various input CW powers for the EOM (P_{EOM}). Depending on the wavelength, normally on and normally off operations appear (separated by the dashed line). Figure 5b shows the optical signal conversion efficiency, η_{conv} . A maximum η_{conv} of 2.3 ± 0.3 (~ 3.6 dB), which means the dynamic signal gain ($\eta_{\text{conv}} > 1$), was successfully obtained for the normally on operation. The maximum η_{conv} for the normally off operation was still as high as 0.6 ± 0.1 . As the peak transmission of the resonance is reduced and redshifted during the modulation as shown in Fig. 2d, the normally off operation is less efficient than the normally on operation. When P_{EOM} becomes too large, the operation becomes unstable because the photocurrents from the PD and the EOM cancel out. Nevertheless, we achieved optical gain, which was also confirmed by the sampled waveforms of the output signal (see Supplementary Section 7). The normally on waveform reveals a steep transition, which might be due to the strong nonlinearity^{27,28}. Despite this nonlinearity, the NRZ modulation for the normally on

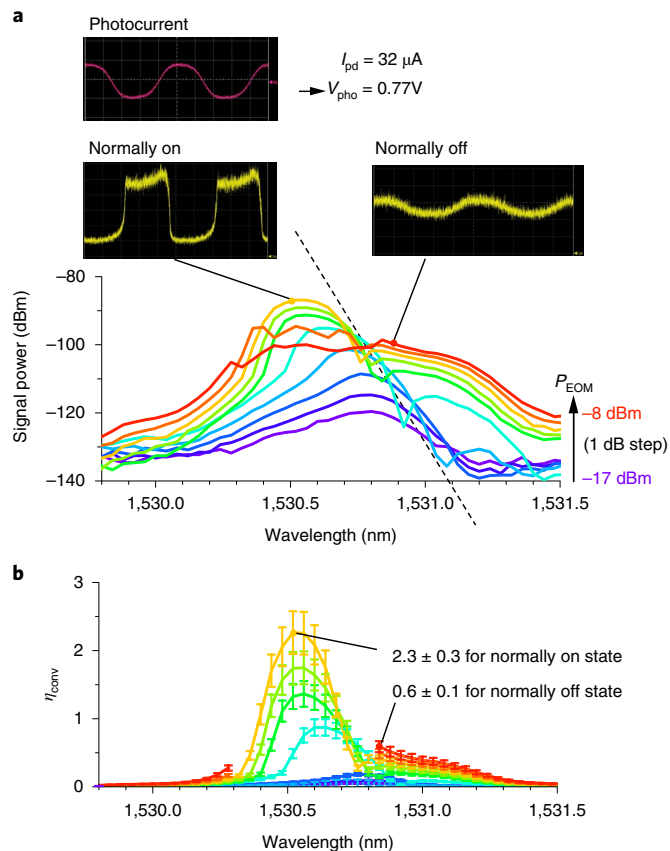


Fig. 5 | Optical signal conversion efficiency. **a**, Signal power spectra detected for the output light from the EOM. The input peak power for the PD is fixed at 32 μ W, which generates a I_{pd} and V_{pho} of 32 μ A and 0.77 V, respectively. Different P_{EOM} curves are shown for -17 dBm to -8 dBm. The signal frequency is 200 MHz. The inset shows the observed waveforms for the photocurrent and the output signal light, indicating the normally on and off states in the modulation. **b**, The efficiency of the optical signal conversion. The plots for the unstable condition are removed.

operation is still as high as 2.5–5 Gbit s^{-1} with optical gain, whereas it is 10 Gbit s^{-1} for the normally off state (see Supplementary Section 11). We speculate that the speed of the normally on operation is restricted by the unintended absorption in the EOM, thereby limiting the speed due to the relatively long carrier lifetime. This could be solved by replacing the embedded InGaAsP with an alternative with a shorter absorption wavelength to operate dominantly with an index modulation in the transparent region.

All-optical switching is an important functionality in photonic processing, and our O–E–O transistors are also superior in terms of the switching performance. The switching energy of our O–E–O transistors is much smaller than those for other all-optical switches (see Supplementary Section 12), with the exception of the purely all-optical PhC-nanocavity switch²⁹. Even against the nanocavity switch, our O–E–O transistor has some advantages. First, the input wavelength range for the PD is very wide, exceeding 80 nm, which provides flexible optical connectivity. Second, a high conversion efficiency and signal gain are difficult to achieve with the purely all-optical nanocavity switch. This offers the possibility of the cascaded connection of multiple devices.

We also compare the performance with the previous O–E–O devices. Some of the previous O–E–O devices (typically self-electro-optic effect devices) have realized optical gain using bistable nonlinearity^{9,12}, but they suffer from speed degradation down to the megahertz region. Other O–E–O devices incorporate optical/

electrical amplifiers or photo-gated transistors to achieve gain with higher speed at the expense of higher electrical energy requirements (picojoules per bit)^{30,31}. Our device does not incorporate any amplifiers, and maintains a high speed (10 Gbit s^{-1}) and a low energy consumption of 4.8 fJ bit⁻¹ (see Supplementary Section 13 for the total efficiency).

There has been much discussion about the roles and limitations of optical transistors in comparison to CMOS transistors³². Although our femtofarad devices can solve some problems posed by previous optical transistors, such as cascading, it is still too early to conclude whether we can replace CMOS transistors with optical ones and such argument is beyond the scope of the present study. Instead, we would like to emphasize that transistor-like operation is useful for improving and expanding various types of optical signal processing.

Outlook

The ultralow-capacitance optoelectronic integration achieved in this work revealed several important prospects in relation to chip-scale information processing. Our nanocavity EOM, with a record-low energy consumption of 42 aJ bit⁻¹, constitutes an energy-efficient optical transmitter. Photodetector–resistor integration offers an amplifier-free photoreceiver. Our PDs are capable of removing the reverse-bias voltage while maintaining high speed³³ and realize a receiver operated without any electrical energy, such as a solar cell. These will be key components for energy-saving dense optoelectronic interfaces with a CMOS layer. There are various applications for the O–E–O transistor with femtojoule per bit energy, which works as an energy-efficient nonlinear element. Many-core CMOS architecture needs to continuously maintain cache coherency³⁴, and hence demands on-chip networking for data broadcasting from one core to all of the other cores. A cascable O–E–O transistor with signal gain would be useful for this purpose. The O–E–O transistor function is also important as an optical repeater, which will play a role in large-scale photonic integration, especially for photonic acceleration in computing. Recently, low-latency optical digital computing^{35,36} and analogue optical computing including photonic neural networks^{37,38} have been proposed, and optical repeaters are key components for establishing scalability to expand their computing capacity. As such, the present femtofarad-level O–E–O/O–E–O components overcome the existing functional limitations in optoelectronic integration, and promise tightly coupled photonic–electronic integrated circuits for new fields of energy-saving information processing.

Data availability

The data that support the plots within this paper and other findings of this study are available from the corresponding author on reasonable request.

Received: 2 November 2018; Accepted: 20 February 2019;
Published online: 15 April 2019

References

- Williams, R. S. What's next? *Comput. Sci. Eng.* **19**, 7–13 (2017).
- Miller, D. A. B. Device requirements for optical interconnects to silicon chips. *Proc. IEEE* **97**, 1166–1185 (2009).
- Miller, D. A. B. Attojoule optoelectronics for low-energy information processing and communications. *J. Lightwave Technol.* **35**, 346–396 (2017).
- Sorger, V. J. et al. Scaling vectors of attojoule per bit modulators. *J. Opt.* **20**, 014012 (2018).
- Krishnamoorthy, A. V. & Miller, D. A. B. Scaling optoelectronic-VLSI circuits into the 21st century: a technology roadmap. *IEEE J. Sel. Top. Quant. Electron.* **2**, 55–76 (1996).
- Timurdogan, E. et al. An ultralow power athermal silicon modulator. *Nat. Commun.* **5**, 4008 (2014).
- Settaluri, K. T. et al. Demonstration of an optical chip-to-chip link in a 3D integrated electronic-photonic platform. In *41st European Solid-State Circuits Conference (ESSCIRC)* 156–159 (IEEE, 2015).

8. Nozaki, K. et al. Photonic-crystal nano-photodetector with ultrasmall capacitance for on-chip light-to-voltage conversion without an amplifier. *Optica* **3**, 483–492 (2016).
9. Lentine, A. L. et al. Symmetric self-electrooptic effect device: optical set-reset latch, differential logic gate, and differential modulator detector. *IEEE J. Quant. Electron.* **25**, 1928–1936 (1989).
10. Kasahara, K. Vstep-based smart pixels. *IEEE J. Quant. Electron.* **29**, 757–768 (1993).
11. Matsuo, S., Amano, C. & Kurokawa, T. Photonic memory switch consisting of multiple quantum-well reflection modulator and heterojunction phototransistor. *Appl. Phys. Lett.* **60**, 1547–1549 (1992).
12. McCormick, F. B. et al. Six-stage digital free-space optical switching network using symmetrical self-electro-optic-effect devices. *Appl. Opt.* **32**, 5153–5171 (1993).
13. Demir, H. V. et al. Multifunctional integrated photonic switches. *IEEE J. Sel. Top. Quant. Electron.* **11**, 86–96 (2005).
14. Matsuo, S., Amano, C. & Kurokawa, T. Operation characteristics of 3-terminal hybrid structure with multiple-quantum-well reflection modulator and heterojunction phototransistor. *IEEE Photon. Technol. Lett.* **3**, 330–332 (1991).
15. Kodama, S. et al. 2.3 picoseconds optical gate monolithically integrating photodiode and electroabsorption modulator. *Electron. Lett.* **37**, 1185–1186 (2001).
16. Nozaki, K. et al. Ultracompact O-E-O converter based on a fF-capacitance nanophotonic integration. In *Conference on Laser and Electro-Optics (CLEO) SF3A.3* (Optical Society of America, 2018).
17. Li, E. W., Gao, O., Chen, R. T. & Wang, A. X. Ultracompact silicon-conductive oxide nanocavity modulator with 0.02 lambda-cubic active volume. *Nano Lett.* **18**, 1075–1081 (2018).
18. Haffner, C. et al. Low-loss plasmon-assisted electro-optic modulator. *Nature* **556**, 483–486 (2018).
19. Nozaki, K. et al. Ultralow-energy electro-absorption modulator consisting of InGaAsP-embedded photonic-crystal waveguide. *APL Photon.* **2**, 056105 (2017).
20. Miller, D. A. B. Energy consumption in optical modulators for interconnects. *Opt. Express* **20**, A293–A308 (2012).
21. Koeber, S. et al. Femtojoule electro-optic modulation using a silicon-organic hybrid device. *Light Sci. Appl.* **4**, e255 (2015).
22. Yoshimatsu, T., Kodama, S., Yoshino, K. & Ito, H. 100-Gb/s error-free wavelength conversion with a monolithic optical gate integrating a photodiode and electroabsorption modulator. *IEEE Photon. Technol. Lett.* **17**, 2367–2369 (2005).
23. Sabnis, V. A. et al. Intimate monolithic integration of chip-scale photonic circuits. *IEEE J. Sel. Top. Quant. Electron.* **11**, 1255–1265 (2005).
24. Nozaki, K., Matsuo, S., Shinya, A. & Notomi, M. Amplifier-free bias-free receiver based on low-capacitance nanophotodetector. *IEEE J. Sel. Top. Quant. Electron.* **24**, 4900111 (2018).
25. Durhuus, T., Mikkelsen, B., Joergensen, C., Danielsen, S. L. & Stubkjaer, K. E. All-optical wavelength conversion by semiconductor optical amplifiers. *J. Lightwave Technol.* **14**, 942–954 (1996).
26. Yamada, K. et al. All-optical efficient wavelength conversion using silicon photonic wire waveguide. *IEEE Photon. Technol. Lett.* **18**, 1046–1048 (2006).
27. Shinya, A. et al. All-optical on-chip bit memory based on ultra high Q InGaAsP photonic crystal. *Opt. Express* **16**, 19382–19387 (2008).
28. Gu, T. et al. Regenerative oscillation and four-wave mixing in graphene optoelectronics. *Nat. Photon.* **6**, 554–559 (2012).
29. Nozaki, K. et al. Sub-femtojoule all-optical switching using a photonic-crystal nanocavity. *Nat. Photon.* **4**, 477–483 (2010).
30. Woodward, T. K. et al. 1-Gb/s two-beam transimpedance smart-pixel optical receivers made from hybrid GaAs MQW modulators bonded to 0.8-μm silicon CMOS. *IEEE Photon. Technol. Lett.* **8**, 422–424 (1996).
31. Dummer, M. M., Klamkin, J., Tauke-Pedretti, A. & Coldren, L. A. 40 Gb/s field-modulated wavelength converters for all-optical packet switching. *IEEE J. Sel. Top. Quant. Electron.* **15**, 494–503 (2009).
32. Miller, D. A. B. Are optical transistors the logical next step? *Nat. Photon.* **4**, 3–5 (2010).
33. Nozaki, K. et al. Forward-biased nanophotonic detector for ultralow-energy dissipation receiver. *APL Photon.* **3**, 046101 (2018).
34. Werner, S., Navaridas, J. & Lujan, M. A survey on optical network-on-chip architectures. *ACM Comput. Surv.* **50**, 89 (2018).
35. Touch, J. et al. Digital optical processing of optical communications: towards an optical turing machine. *Nanophotonics* **6**, 507–530 (2017).
36. Ishihara, T., Shinya, A., Inoue, K., Nozaki, K. & Notomi, M. An integrated nanophotonic parallel adder. *ACM J. Emerg. Technol. Comput. Syst.* **14**, 1–20 (2018).
37. Tait, A. N. et al. Neuromorphic photonic networks using silicon photonic weight banks. *Sci. Rep.* **7**, 7430 (2017).
38. Shen, Y. C. et al. Deep learning with coherent nanophotonic circuits. *Nat. Photon.* **11**, 441–446 (2017).
39. Ren, S. et al. Ge/SiGe quantum well waveguide modulator monolithically integrated with SOI waveguides. *IEEE Photon. Technol. Lett.* **24**, 461–463 (2012).
40. Haffner, C. et al. All-plasmonic Mach-Zehnder modulator enabling optical high-speed communication at the microscale. *Nat. Photon.* **9**, 525–518 (2015).
41. Sorger, V. J., Lanzillotti-Kimura, N. D., Ma, R. M. & Zhang, X. Ultra-compact silicon nanophotonic modulator with broadband response. *Nanophotonics* **1**, 17–22 (2012).
42. Srinivasan, S. A. et al. 56 Gb/s germanium waveguide electro-absorption modulator. *J. Lightwave Technol.* **34**, 419–424 (2016).

Acknowledgements

We thank J. Asaoka, H. Onji, Y. Shouji and K. Ishibashi for their support in fabricating the device. This work was supported by CREST (JPMJCR15N4), the Japan Science and Technology Agency.

Author contributions

K.N. designed the devices and performed the measurements. S.M., T.F. and K.T. supported the design and fabrication of the samples. A.S. and E.K. supported the design and fabrication of the photonic-crystal structure. M.N. led the project. K.N. and M.N. conceived and planned this work, analysed the data and wrote the manuscript.

Competing interests

The authors declare no competing interests.

Additional information

Supplementary information is available for this paper at <https://doi.org/10.1038/s41566-019-0397-3>.

Reprints and permissions information is available at www.nature.com/reprints.

Correspondence and requests for materials should be addressed to K.N. or M.N.

Publisher's note: Springer Nature remains neutral with regard to jurisdictional claims in published maps and institutional affiliations.

© The Author(s), under exclusive licence to Springer Nature Limited 2019